Bulletin of Volcanology (2026) 88:109
https://doi.org/10.1007/s00445-026-02032-1

RESEARCH

Integrated geodetic and seismic constraints on deformation at Nevados de Chillán, 2015–2025

Blanca Symmes-Lopetegui[1,3] · Francisco Delgado[2] · Sabrina Metzger[1] · Sergio Ruiz[3] · Juan Carlos Báez[4] · Leoncio Cabrera[5] · Shaoyang Li[6] · Alex Alarcón[7]

Received: 24 April 2026 / Accepted: 17 August 2026
© The Author(s) 2026

Abstract

The Nevados de Chillán Volcanic Complex in the Southern Volcanic Zone (SVZ) of the Andes is one of the most active volcanic systems in Chile and has recently hosted one of the longest and best-instrumented eruptive cycles documented in the country. Here, we integrate satellite-geodetic and seismic time series spanning December 2015 to late 2025 to characterize the full eruptive cycle. We identify three main periods: (I) slight subsidence from 2015 to 2019, (II) marked inflation from 2019 to 2022 with a maximum LOS displacement of ∼25 cm, and (III) deflation from late 2022 onward. Inflation and deflation produced a similar spatial pattern with opposite sign and a cumulative LOS range change of ∼20 cm. We modeled the 2019–2022 inflation using a pressurized prolate spheroid and found that deformation throughout all three periods was mainly associated with a shallow source region centered at ∼5.4 km depth. The source aligns with the NW-SE-oriented Cortaderas Lineament and volcano-tectonic seismicity at 3–6 km depth. The volcano continued to inflate during the period of highest effusive output, while erupted lava volumes remained modest relative to the modeled source volume change, suggesting continued pressurization. Seismicity migrated northeastward during Period II, indicating structural control on shallow magma storage and transport. Through late 2025, deformation and seismicity declined toward pre-eruptive background conditions.

Keywords Nevados de Chillán · Volcanic processes · Kinematic source modeling · Seismicity · GNSS · InSAR

Editorial responsibility: F. Galetto

✉ Blanca Symmes-Lopetegui
bsymmes@gfz.de

Francisco Delgado
fdelgado@uchile.cl

Sabrina Metzger
sabrina.metzger@gfz.de

Sergio Ruiz
sruiz@uchile.cl

Juan Carlos Báez
jcbaez@csn.uchile.cl

Leoncio Cabrera
leoncio.cabrera@uc.cl

Shaoyang Li
shaoyangli@mail.iggcas.ac.cn

Alex Alarcón
alex.alarcon@sernageomin.cl

1 Lithosphere Dynamics, Helmholtz Centre Potsdam, GFZ German Research Centre for Geosciences, Potsdam, Germany

Introduction

Chile hosts one of the most active volcanic arcs worldwide with ∼100 active volcanoes (Lara et al. 2011), offering exceptional conditions to study the temporal evolution of magmatic and eruptive processes in subduction zones (Galetto et al. 2023; Delgado et al. 2025). The Southern

2 Departamento de Geología, Facultad de Ciencias Físicas y Matematicas, Universidad de Chile, Santiago, Chile

3 Departamento de Geofísica, Facultad de Ciencias Físicas y Matematicas, Universidad de Chile, Santiago, Chile

4 Centro Sismologico Nacional, Universidad de Chile, Santiago, Chile

5 Departamento de Ingeniería Estructural y Geotécnica, Pontificia Universidad Catolica de Chile, Santiago, Chile

6 State Key Laboratory of Lithospheric and Environmental Coevolution, Institute of Geology and Geophysics, Chinese Academy of Sciences, Beijing 100029, China

7 Southern Andean Volcano Observatory, Geological and Mining Chilean Service, Temuco, Chile

Published online: 03 September 2026

Volcanic Zone (SVZ) between 33°S and 46°S includes at least 60 historically and potentially active volcanic edifices (Simkin 1994; Stern 2004; Delgado et al. 2017; Cabrera et al. 2024). Among the most active are the Laguna del Maule, Nevados de Chillán, Villarrica, and Puyehue-Cordón Caulle volcanic complexes (Delgado et al. 2025; Cortés et al. 2024; Le Mével et al. 2021; Navarrete-Reyes et al. 2026). But eruptive cycles over their full duration have rarely been continuously monitored with modern geodetic and seismic networks, limiting our understanding of how deformation and seismicity evolve through long-lived eruptive cycles.

We focus on the Nevados de Chillán Volcanic Complex (NChVC), located in the Ñuble Region (36°51'S; 71°24'W, 3216 m.a.s.l., Fig. 1), which has been active for ~650 ka (Dixon et al. 1999), comprises seventeen emission centers aligned predominantly along a NW-SE direction (Orozco et al. 2016; Cardona et al. 2021; Mura et al. 2025), and has been permanently monitored since 2012 by the Southern Andean Volcano Observatory (OVDAS) that is operated by the Geological and Mining Chile Service (Servicio Nacional de Geología y Minería (SERNAGEOMIN) 2026; Orozco et al. 2016). The December 2015 to January

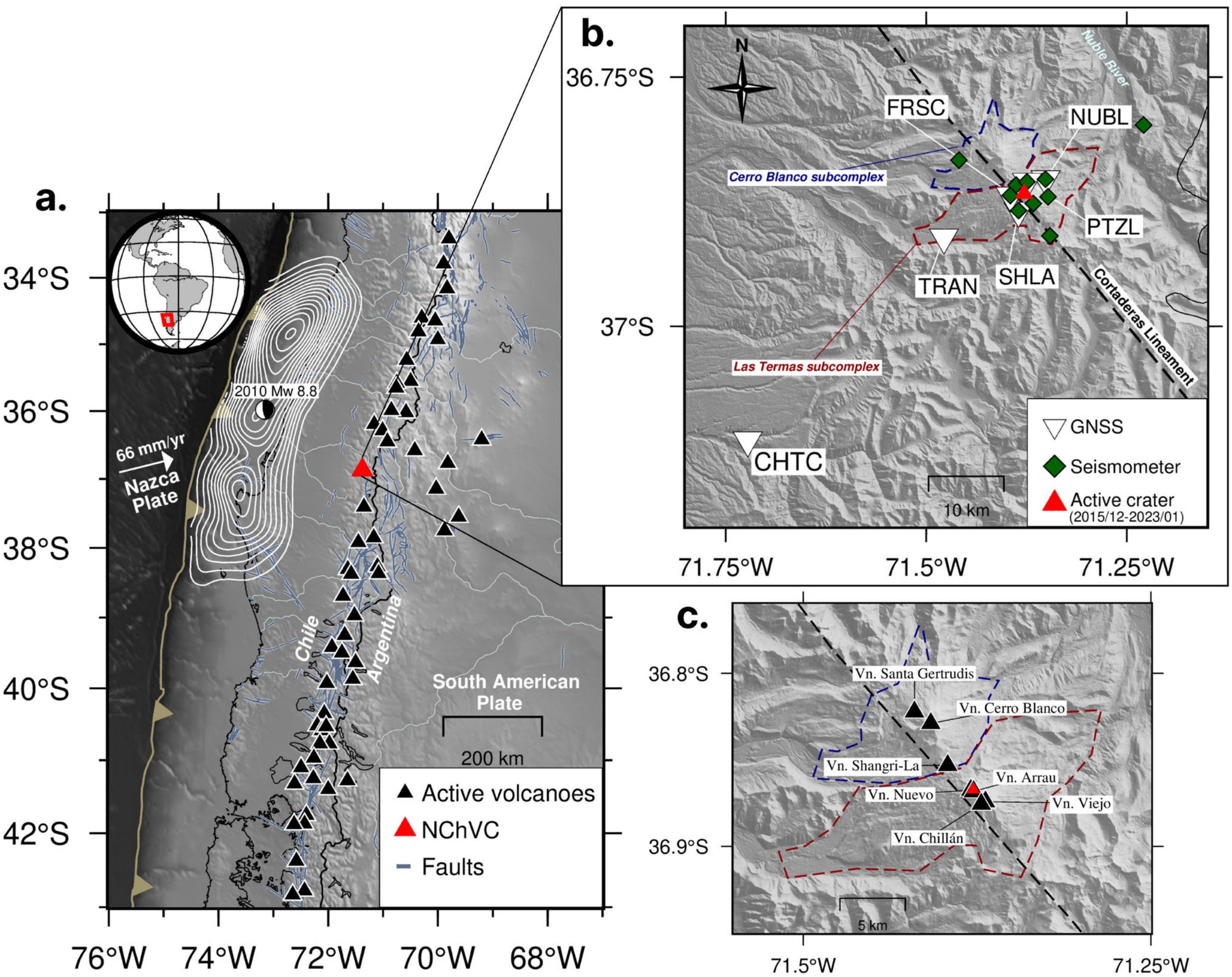

Fig. 1 **a** Regional map showing the location of the Nevados de Chillán Volcanic Complex (NChVC; red triangle) within the active volcanic arc of Chile (black triangles). The triangulated line marks the Chilean subduction zone, and the black onshore line marks the Chile-Argentina border. White contours mark the rupture extent of the 2010 Maule earthquake (Mw 8.8) (Moreno et al. 2012), and faults are shown in blue (Maldonado et al. 2021). **b** Local map of our study area showing the active Nicanor crater (red triangle; 2015/12–2023/01), seismic stations (green diamonds), GNSS stations (white inverted triangles). The black dashed line marks the Cortaderas Lineament, which aligns several cones and craters (Cardona et al. 2021; Mura et al. 2025; Espinosa-Leal et al. 2025). **c** Close-up view of the NChVC showing the individual volcanic edifices of the Cerro Blanco subcomplex (Vn. Santa Gertrudis, Vn. Cerro Blanco, Vn. Shangri-La) and the Las Termas subcomplex (Vn. Nuevo, Vn. Arrau, Vn. Viejo, Vn. Chillán) (Pineda et al. 2025)

2023 eruptive cycle stands out as one of the longest and the best-instrumented sequences documented in Chile, providing an opportunity to track a magmatic system from early unrest through post-eruptive relaxation. Beyond the distinct surface deformation, the eruptive cycle was also marked by pronounced changes in seismicity. The volcano's reactivation was characterized by increasing long-period (LP) activity together with more regular volcano-tectonic (VT) seismicity, and VT hypocenters were described along a NW-SE structural trend consistent with the Cortaderas Lineament (Cardona et al. 2021). Later effusive phases were accompanied by increased seismicity, including a rise in VT earthquake rate at the onset of the 2019 uplift episode (Eiden et al. 2025).

Recent studies have used Sentinel-1 InSAR and GNSS observations to characterize parts of the 2019–2022 uplift episode and to model the responsible deformation source. Astort et al. (2022) modeled a pressurized prolate spheroid at $\sim$5.5 $\pm$ 0.5 km beneath the Las Termas subcomplex using Sentinel-1 data from October 2019 to November 2020, consistent with the NW-SE Cortaderas Lineament (Cardona et al. 2021; Mura et al. 2025). Lizama et al. (2025) proposed instead a two-reservoir system using ascending ALOS-2 and descending Sentinel-1 data from January 2019 to May 2020, with a shallow source at $\sim$5.8 km and an additional deeper sill at $\sim$15 km. Eiden et al. (2025) interpreted the deformation as a sequence of independent inflation episodes, obtaining source depths ranging from $\sim$4.3 to $\sim$6.4 km across three sub-periods: Uplift 1 (July 2019–July 2020), Uplift 2 (October 2020–May 2021), and Uplift 3 (August 2021–January 2022), using InSAR and GNSS. These studies consistently document inflation since 2019 but differ in source depth and geometry, rely primarily on Sentinel-1 data with limited coherence over the densely vegetated volcanic flanks, and cover only portions of the eruptive sequence.

We present continuous GNSS displacement time-series at six stations, including five near-field stations and a reference station (CHTC), ALOS-2 and Sentinel-1 InSAR time-series, a SAOCOM-1 interferogram, and a seismic event catalog spanning the full eruptive cycle and subsequent post-eruptive evolution of NChVC from 2015 to late 2025. By extending the analysis through late 2025 and integrating coherent L-band radar data, which are better suited to monitor displacement in the densely vegetated volcanic terrain typical of the Southern Andes (e.g., Delgado et al. (2024)), we provide the most complete geodetic and seismic characterization of NChVC to date, extending the temporal and spatial coverage achieved by previous studies. We employ a pressurized prolate spheroid model (Yang et al. 1988) to characterize a source geometry and depth capable of reproducing the first-order deformation pattern observed across the three periods of the cycle. In addition, we discuss the implications for magma storage, recharge dynamics, and post-eruptive evolution.

Nevados de Chillán volcanic complex (NChVC)

Historical eruptions

The NChVC is one of the most active and hazardous volcanic complexes in Chile (Lara et al. 2011; Servicio Nacional de Geología y Minería (SERNAGEOMIN) 2026), owing to its proximity to human settlements and tourist infrastructure. More than 15 historical eruptions, including both explosive and effusive activity, have been documented (Dixon et al. 1999; Orozco et al. 2016). The NChVC consists of two subcomplexes separated by approximately 6 km: the predominantly andesitic Cerro Blanco subcomplex to the northwest and the predominantly dacitic Las Termas subcomplex to the southeast (Fig. 1b, c) (Naranjo and Moreno 2009). Historical activity has been concentrated within the Las Termas subcomplex, which includes the Nuevo, Arrau, Viejo, and Chillán volcanic centers (Fig. 1c) (Orozco et al. 2016). The Viejo stratocone (Vn. Viejo in Fig. 1c) is the oldest of these edifices and was active between approximately 9.3 and 2.3 ka. The dacitic Chillán cone (Vn. Chillán in Fig. 1c) last erupted in 1883 (Moussallam et al. 2018; Naranjo et al. 1994; Brüggen 1948).

The seventeen emission centers of NChVC are aligned along a NW-SE arc-oblique volcanic lineament structurally related to the Andean Transverse Fault system (Mura et al. 2025; Stanton-Yonge et al. 2016). This lineament might mark a northwestern continuation of the $\sim$200 km long Cortaderas Lineament, a crustal discontinuity extending from the Chilean Cordillera into the Argentine foreland. The discontinuity has been active since at least the Paleocene (Ramos and Barbieri 1989; Ramos and Folguera 2005; Radic 2010), though the precise nature of this connection remains poorly constrained (Mura et al. 2025). The structure is transverse to the volcanic arc and oblique to the prevailing interseismic stress field, though coseismic rebound during megathrust events can transiently promote magma ascent along NW-striking structures (Stanton-Yonge et al. 2016). The lineament directly controls the distribution of eruptive centers and geometry at NChVC (Cardona et al. 2021; Mura et al. 2025; Espinosa-Leal et al. 2025).

The Nuevo volcano (Fig. 1c) was formed during activity between 1906 and 1948 (volcanic explosivity index VEI 2, Global Volcanism Program) and included lava flows, eruptive plumes, seismicity, intermittent explosive phases, and a late effusive phase producing lahars (Orozco et al. 2016). Between 1973 and 1987 (VEI 2), the Arrau volcano (a dacitic lava cone) formed from dome growth. This period involved successive eruptive pulses and gravitational collapses in addition to gas and ash emissions (Naranjo et al. 1994, 2008; Orozco et al. 2016). Nuevo and Arrau volcanoes were emplaced on top of the Democrático volcano (Dixon et al. 1999). More recently, in August–September 2003 (VEI 0–1), a small Vulcanian-type eruption generated the double Chudcún crater, and in 2008 (VEI $\leq$ 1) a lava flow was observed to the NE of the Nuevo volcano from the new San Sebastián center (Naranjo and Moreno 2009).

The last activity at NChVC occurred immediately after the 2010 M_w 8.8 Maule megathrust earthquake that ruptured a ~500 km-long plate interface segment at ~150 km distance (Fig. 1) (Moreno et al. 2012). The postseismic viscoelastic relaxation following this event produced long-wavelength surface deformation that was still ongoing at least 8 years after the earthquake and might affect our study area (Li et al. 2017, 2018). Within weeks of the earthquake, Pritchard et al. (2013) documented up to 15 cm of coseismic subsidence at NChVC, attributed to the release of hydrothermal fluids from a reservoir at 3–10 km depth; new non-eruptive fumarolic activity was also reported at the volcano three days after the event, suggesting that the earthquake transiently destabilized the shallow hydrothermal system.

The 2015–2023 eruptive activity

The most recent and most intensively monitored eruptive episode began in December 2015 and was classified as VEI 2 (Global Volcanism Program). It includes the episodes shown in Table 1:

Table 1 Chronology of the 2015–2023 eruptive activity (VEI 2). Source: Sernageomin Timeline and Global Volcanism Program

Year	Activity summary
2015	Anomalous seismicity
2016	Increased seismic activity, beginning of a period of explosive events, formation of new craters
2017	Phreatic and phreatomagmatic explosions, formation of the Nicanor crater. In December, emission of the Gil Cruz lava dome inside the Nicanor crater
2018	Partial destruction and re-generation of the Gil Cruz dome, pyroclastic flows
2019	Four lava flows (L1, L2, L3, and L4) from the Nicanor crater
2020	Intermittent explosions with ash plumes and pyroclastic flows (late January to early June); lava dome growth and a lava flow on the northern flank (from late June on)
2021	Lava flows L5 and L6 and creation of a second dome (early in the year), highest eruptive rate at Nicanor crater with an effusive period marked by the emission of dome 3 and lava flows L7 and L8 (end of the year)
2022	Emission of the fourth dome, explosive phase with column heights >2 km and short-range pyroclastic flows, last recorded surface activity (October 17)
2023	Decrease in seismic energy, end of the eruptive cycle

During the eruptive episode at the NChVC (December 2015 to January 2023), seismic stations recorded approximately 520,000 earthquakes; four domes were emplaced in the Nicanor crater and subsequently destroyed and cumulative SO2 emissions exceeded 580 kt (Servicio Nacional de Geología y Minería (SERNAGEOMIN) 2026). As of late 2025, seismic monitoring shows low-level background seismicity with occasional events and no sustained surface activity. Based on the geodetic time series ("Geodetic data" section), we distinguish three deformation periods over the observed record: Period I, characterized by slight subsidence (2015/12/18–2019/01/25); Period II, characterized by marked inflation (2019/01/25–2022/03/04); and Period III, characterized by deflation (2022/03/04–2025/02/28).

Data analysis and modeling

We integrated seismic catalogs with surface displacements derived from GNSS and InSAR (ALOS-2, SAOCOM-1, and Sentinel-1) time-series spanning 10 and 8 years, respectively, to characterize the deformation cycle at NChVC. We modeled the observed uplift using a pressurized prolate spheroid to constrain the geometry and depth of the magmatic source, as described below.

Seismic data

The seismic catalog for NChVC spans January 2014 to late 2025 and is routinely compiled by OVDAS (Servicio Nacional de Geología y Minería (SERNAGEOMIN) 2026). It includes hybrid (HB) events related to mixed brittle and fluid-driven processes, long-period (LP) events associated with fluid dynamics, seismic tremor (TR) reflecting sustained fluid or magma movement, and volcano-tectonic (VT) events related to brittle rock failure (Fig. 2). We focus mostly on VT events because they have reliable hypocentral locations; LP, TR, and HB events are routinely detected but poorly constrained in depth and location. The largest reported local magnitude in the VT catalog is 4.6 M_L (Figs. 2, 3, and S1), and the completeness magnitude is approximately 1.0 M_L, consistent with the Gutenberg-Richter frequency-magnitude distribution.

We computed the b-positive parameter following the approach of Van Der Elst (2021), which is based on the distribution of positive magnitude differences between successive events. For this, we used a moving window of 200 VT events, advancing the window one event at a time along the catalog (Fig. 2). Within each window, we calculated the differences in magnitude between consecutive events and retained only those exceeding a minimum threshold of $\Delta M = 0.2$, consistent with discretized magnitude catalogs.

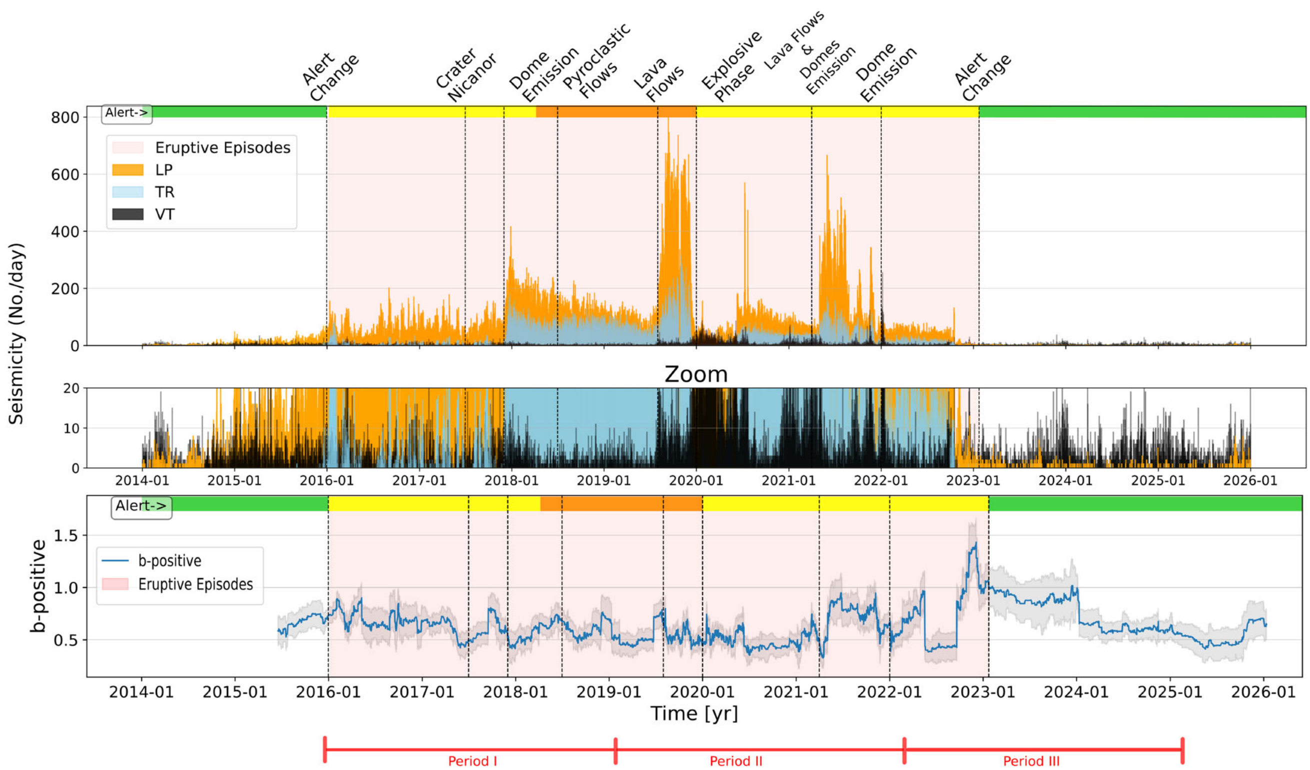

Fig. 2 Upper panel: Daily seismicity at the NChVC from 2014 to 2025, with LP (long-period) events shown in orange, TR (tremor) in gray-blue, and VT (volcano-tectonic) in black. A zoomed-in section below highlights periods of increased VT activity. Lower panel: Temporal evolution of the b-positive parameter calculated from volcano-tectonic (VT) seismicity only (in blue, uncertainty range in gray). Both panels illustrate the variability of eruptive processes (Table 1) and corresponding Sernageomin-OVDAS alert levels (green: no significant change in activity; yellow: volcanic unrest with minor activity changes; orange: significant unrest with possible increase in activity) throughout the observation period

GNSS

We processed data from six continuous GNSS stations covering December 2015 to late 2025 (Fig. 1). The stations are operated by OVDAS and the National Seismological Center (CSN) of the University of Chile and were processed using a differential strategy with Bernese software V5.4 (Dach et al. 2007; Báez et al. 2018). Station CHTC, located approximately 40 km southwest of NChVC, was selected as a local reference because it lies outside the volcanic deformation field.

The horizontal trajectories shown in Figs. 4a–c and the time series in Fig. S2 correspond to the original GNSS solutions. For Fig. 4d and for comparisons with the InSAR observations and model predictions, we subtracted the east, north, and vertical components recorded at CHTC from the corresponding components at the other stations. For the LOS comparisons, these relative GNSS displacements were projected into the corresponding satellite line of sight (Figs. 6, S4, and S5).

InSAR

We acquired radar imagery from three satellite missions: ALOS-2 and SAOCOM-1 in L-band, and Sentinel-1 in C-band. The L-band observations provide improved coherence over highly vegetated regions.

We used ALOS-2 imagery acquired in Stripmap Mode 3 (SM3 10 m/pixel) on an ascending orbit, beams F2-F6, from December 18, 2015, to February 28, 2025, with one radar image per year (Fig. S6). We discarded the image acquired in 2014 due to an incorrect center frequency setting. We created the interferograms using the *alosStack.py* workflow (Liang and Fielding 2017a, b) implemented in the InSAR Scientific Computing Environment (ISCE2) software (Rosen et al. 2012). We considered a maximum temporal baseline of 2.5 years, and built connections with the two previous and two following images. We used the 30 m Copernicus DEM from the European Space Agency to remove the topographic phase. Before processing, the DEM elevations were converted from the EGM2008 geoid to WGS84 ellipsoidal

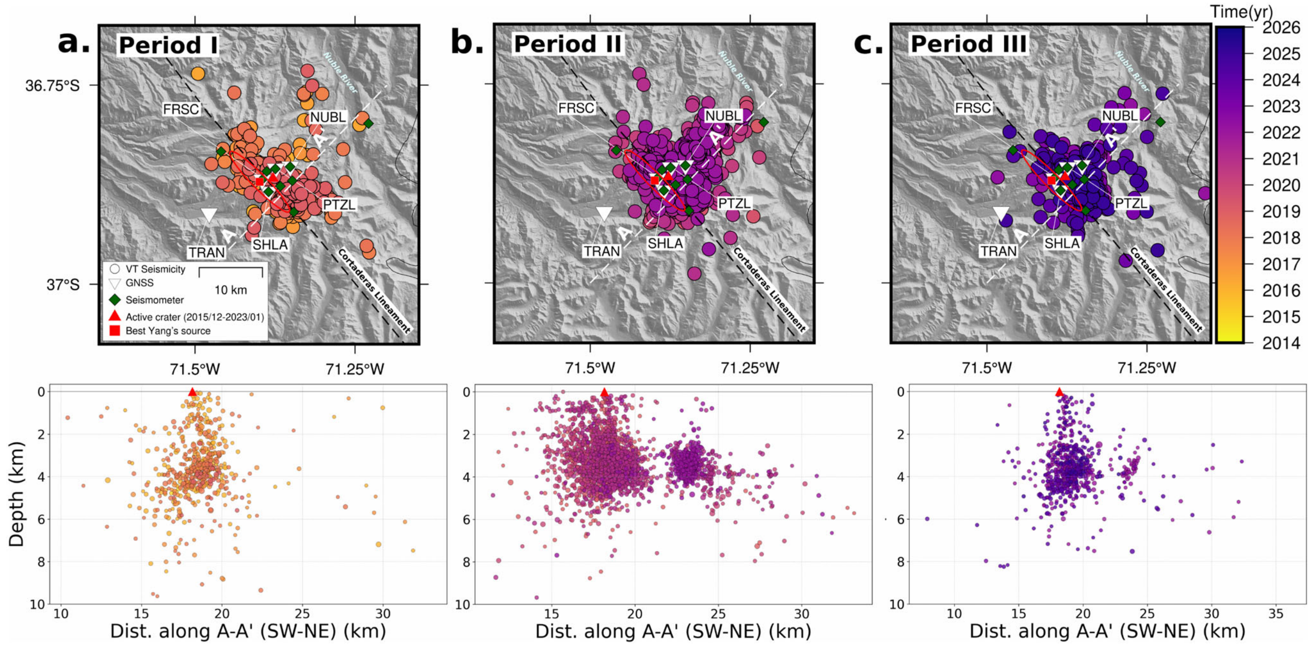

Fig. 3 Map view (top panels) and SW–NE cross section (bottom panels) of volcano-tectonic (VT) seismicity for three periods: **a** 2015–2019, **b** 2019–2022, and **c** 2022–2025. Colors indicate progression over time. Inverted white triangles mark GNSS stations, green diamonds represent seismometers, and the red triangle indicates the active crater location, shown in both map view and projected onto the cross-section profile. The red square marks the preferred prolate spheroid source location. The black dashed line marks the Cortaderas Lineament. White dashed lines in map view indicate the location of the SW–NE cross section A–A'

heights. We then averaged the interferograms using 8 looks in range and 16 looks in azimuth. We applied the split-spectrum technique to remove the ionospheric phase (Rosen et al. 2010; Gomba et al. 2015; Liang et al. 2018), an adaptive phase filter (Goldstein and Werner 1998) with a power spectrum coefficient of 0.5, and unwrapped the phase using Minimum Cost Flow (MCF) (Chen and Zebker 2002). We built a small-baseline (SBAS) InSAR time-series and derived the cumulative deformation with MintPy (Miami InSAR Time-series software in Python) (Yunjun et al. 2019).

We processed one descending SAOCOM-1 interferogram spanning October 2019–November 2021 (Fig. 5), using the *stripmapApp.py* workflow in ISCE2 (Rosen et al. 2012). Pixels were averaged with 8 looks in range and 16 in azimuth, and the topographic phase was removed using the 30 m Copernicus DEM. We applied a phase filter with a power spectrum coefficient of 0.5 (Goldstein and Werner 1998) and removed a linear ramp to account for ionospheric and tropospheric long-wavelength signals (Delgado et al. 2024).

We used automatically processed Sentinel-1 C-band interferograms (Lazecký et al. 2020) from descending track 83, from October 2014 until June 2023, and formed a network of interferograms with temporal baselines ranging from 6 days to 1 year (Fig. S6). Pixels were averaged with 4 looks in azimuth and 20 looks in range, and the topographic phase was removed using the 1 arc-second, void-filled Shuttle Radar Topography Mission (SRTM) DEM (Farr et al. 2007). We applied an adaptive phase filter (Goldstein and Werner 1998) with an FFT window size of 32 and a power spectrum coefficient of 1.0, unwrapped the phase with Minimum Cost Flow (MCF) (Chen and Zebker 2002), and masked pixels with coherence below 0.5. We built InSAR time-series (Fig. S5) with the open-source SBAS analysis tool LiCSBAS (Morishita et al. 2020), which includes an atmospheric correction (Yu et al. 2017, 2018). We manually excluded incoherent interferograms, particularly during the austral winter period.

For comparison with the GNSS observations, the ALOS-2 time series were referenced using the location of the CHTC GNSS station. Since CHTC lies outside the Sentinel-1 coverage, the Sentinel-1 time series were referenced to a stable area shown in Fig. S5.

Source modeling

To constrain the location and geometry of the magmatic source driving surface uplift, we used a pressurized finite prolate spheroid model (Yang et al. 1988), inverting the cumulative LOS displacement maps derived from the ALOS-2 and SAOCOM-1 L-band datasets during Period II (2019–2022), which provide the most complete and coherent spatial coverage over the vegetated flanks of the volcano. Sentinel-1 was not included in the inversion because of its higher noise

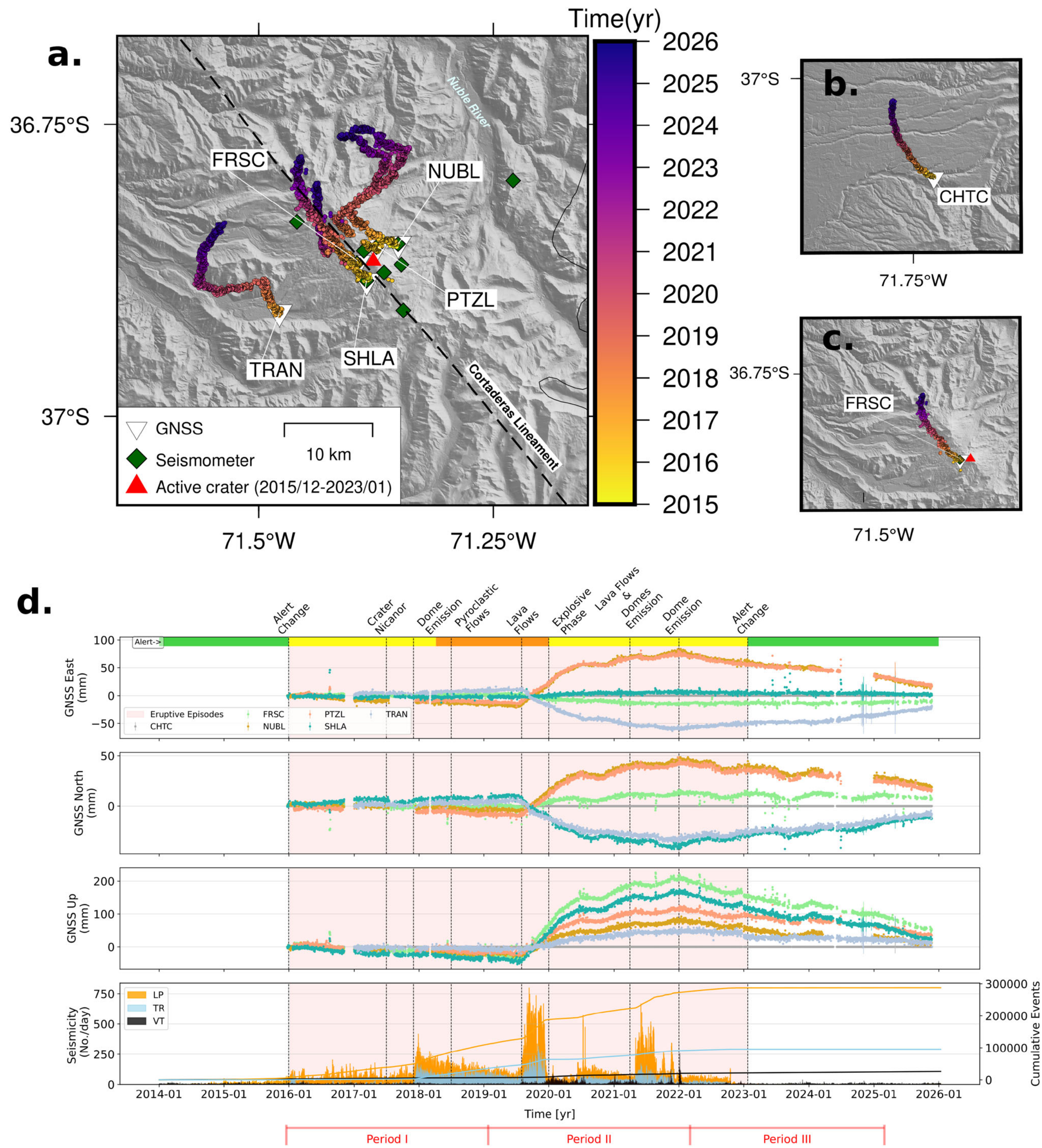

Fig. 4 **a** Map showing the monitoring network around the active crater (red triangle), including seismometers (green diamonds) and GNSS stations (inverted triangles). The colored trajectories represent the original cumulative horizontal GNSS displacements, color-coded by time. Insets show the original horizontal displacement trajectories at **b** CHTC and **c** FRSC. **d** East, North, and vertical GNSS time series at all six stations, referenced to CHTC and color-coded by Sernageomin-OVDAS alert levels (as in Fig. 2). The bottom panel shows seismicity as in Fig. 2, together with the cumulative number of events over the same period

level and reduced coherence in parts of the study area. The GNSS stations are sparse and unevenly distributed around the deformation source and therefore provide limited constraints on its geometry. Sentinel-1 and GNSS were retained as independent observations for comparison. To reduce data redundancy while preserving the spatial characteristics of the deformation signal, the InSAR displacement maps were spatially downsampled using a resolution-based approach (Lohman and Simons 2005).

Using the Neighborhood Algorithm, we initially searched for the source centroid location, major semi-axis, dip, and strike (Fig. S7). During repeated preliminary inversion runs, the strike was left as a free parameter and consistently converged toward 134°. The strike was therefore fixed at this value in the final inversions. The minor semi-axis was fixed at 1 km in all inversions to ensure that the radius of curvature of the upper surface of the spheroid does not exceed its depth below the surface. Parameter uncertainties for the remaining free parameters (centroid location, major semi-axis, and dip) were estimated from the spread of multiple Neighborhood Algorithm runs (Fig. S7).

Model performance was evaluated using the mean squared misfit, calculated as the sum of the squared residuals divided by the number of observations. We assumed a shear modulus of $\mu = 2.1$ GPa, consistent with values commonly adopted for volcanic rocks (Heap et al. 2020). The pressure change ΔP was solved independently for each InSAR dataset via least-squares, and the corresponding volume change was derived from the estimated ΔP and the assumed μ following Yang et al. (1988). We simultaneously solved for a linear ramp to account for any residual long-wavelength signal in the InSAR data and to adjust the reference point. The fit to the independent Sentinel-1 and GNSS observations was subsequently used to evaluate the preferred model.

After obtaining the preferred source geometry for Period II, we fixed it and performed forward calculations for Period I (2015–2019) and Period III (2022–2025), estimating only ΔP via least-squares inversion of the cumulative ALOS-2 displacement maps. This allowed us to test whether the Period II geometry reproduces the first-order deformation patterns observed during the other two periods.

Results

As introduced in the "The 2015–2023 eruptive activity" section, our observations define three distinct seismo-geodetic activity phases at NChVC: a prolonged pre-event Period I (2015–2019), characterized by background seismicity and subtle localized subsidence; event Period II (2019–2022), marked by increased volcano-tectonic (VT) seismicity and surface deformation consistent with inflation; and post-event Period III (2022–2025), during which seismic activity declined and the deformation signal reversed sign, indicating deflation. Period boundaries are defined by the available ALOS-2 acquisition dates which are closest to the onset of the observed seismic and geodetic changes. InSAR observations extend through February 2025, whereas GNSS and seismic data extend through late 2025. In the following, we describe the temporal and spatial evolution of seismicity ("Seismicity" section), the space-geodetic observations ("Geodetic data" section), and the source-modeling results ("Source modeling" section).

Seismicity

Period I (2015–2019)

Seismic activity slowly but significantly increased during 2015 until the end of the year, when the alert level was raised from green to yellow. During 2016, more than 1,200 seismic events were recorded, dominated by long-period (LP) and tremor (TR) activity associated with the onset of explosive episodes and formation of new craters; volcano-tectonic (VT) earthquakes were also present but less frequent (Fig. 2). LP and TR activity remained elevated through 2016 and 2017, including a marked increase in LP events by the end of 2017, coincident with the onset of new crater activity and subsequent lava-dome emplacement. From 2018 onward, LP and TR seismicity showed a sudden, sustained increase, and VT hypocenters progressively aligned along a NW-SE trend (Figs. S1 and 3).

Period II (2019–2022)

Between late 2019 and 2020, seismic activity increased across all event types (LP, TR, VT), coinciding with the effusion of lava flows (Fig. 2), with LP and TR dominating throughout. A second seismic peak of LP and TR between 2021 and 2022 was associated with renewed dome emplacement and effusive activity. VT earthquakes increased in discrete pulses toward the end of 2019, 2021, and 2022, each coinciding with eruptive episodes, but remained less numerous than LP events throughout the period.

During 2020–2022, VT hypocenters migrated progressively northeastward relative to the active crater (Fig. 3), culminating in January 2022 with a pronounced cluster $\sim$5 km northeast of the crater at 3–4 km depth (Figs. S1 and 3). Most VT events occurred at depths of 3–6 km (Fig. 3).

Period III (2022–2025)

Eruptive activity declined markedly by late 2022, with partial destruction of the dome in August 2022 and the last recorded eruptive event in October 2022. From November 2022, TR and LP seismicity decreased substantially: TR events declined toward year-end, while VT and LP events returned to background levels through 2023 (Fig. 2). The alert level was downgraded to green in January 2023.

The b-positive parameter, estimated from the VT catalog, fluctuated between 0.5 and 1.5 throughout the study period, with a marked increase in May 2022 concurrent with the largest-magnitude event of the eruptive cycle (M_L 4.6; Fig. 2). Through 2024 and into late 2025, seismicity remained low, dominated by VT and LP events (Fig. 2).

Geodetic data

Period I (2015–2019): Gradual displacement

The East, North, and vertical GNSS components show slow and almost linear displacements, consistent with a subtle subsidence signal observed in the InSAR. This localized subsidence near the active crater is consistently captured by GNSS and InSAR and is most clearly expressed in the time-series of GNSS station FRSC projected into the LOS (Fig. 6), with a rate of less than 1 cm/yr. The signal is also visible in both ALOS-2 and Sentinel-1 time-series, the latter with a higher temporal sampling (Figs. 6 and S5).

Period II (2019–2022): Inflation

The GNSS time-series record an abrupt rate change corresponding to inflation that begins in late 2019 and continues through 2020. The strongest deformation is centered at and around the active crater (Fig. 6). Station FRSC, located closest to the active crater, records approximately 22.5 cm of vertical uplift (Fig. 4) in this period but shows no significant horizontal displacement attributable to the inflation. PTZL and NUBL move towards NE, the other stations all move towards WNW, and only CHTC remains unaffected (Fig. 4). All stations exhibited a non-linear, rapid uplift in 2019–2020 that, in the case of TRAN, was captured by an exponential fit (Fig. S3). Radar interferometry of three satellite missions all captures this deformation (Figs. 5 and 6). ALOS-2 and SAOCOM-1 both record cumulative LOS displacements exceeding ∼25 cm, consistent with the GNSS displacement at FRSC. The scatter between the ALOS-2 and GNSS LOS time-series is ∼10 mm (Fig. 6), which we consider a proxy for the remaining noise in the ALOS-2 displacement maps. Sentinel-1 resolves the same deformation pattern (Fig. S5), although at lower amplitudes, likely due to its higher noise level and shorter observation period, which extends only to June 2023. In contrast, ALOS-2 observations extend to February 2025, although with approximately one acquisition per year.

Period III (2022-2025): Transition to deflation

The beginning of this period is marked by a transition from inflation to deflation processes as indicated in both GNSS and InSAR observations. Vertical GNSS components record a deflation trend (Fig. 4) similar to the one observed in the InSAR LOS signal, with a quasi-linear peak decay rate of approximately −5 cm/yr (Fig. 6).

Source modeling

The preferred prolate spheroid for Period II is centered at 5.4 ± 0.2 km depth at 71.40°W, 36.87°S, near GNSS station FRSC and beneath the active crater, with a major semi-axis of 5.9 ± 0.1 km, a fixed minor semi-axis of 1 km, a fixed NW–SE strike of 134° clockwise from North, and a near-horizontal dip of 3°–8° along the major axis. The fixed strike is consistent with the value obtained during the preliminary inversions (134 ± 1°). The estimated volume changes are 0.048 km^3 during the ALOS-2 observation period (2019/01/25 − 2022/03/04) and 0.028 km^3 for the SAOCOM-1 period (2019/10/25 − 2021/11/07).

The predicted LOS displacements reproduce well the observed deformation pattern in both datasets (Fig. 7), with RMS residuals of 1.5 cm for ALOS-2 and 1.6 cm for

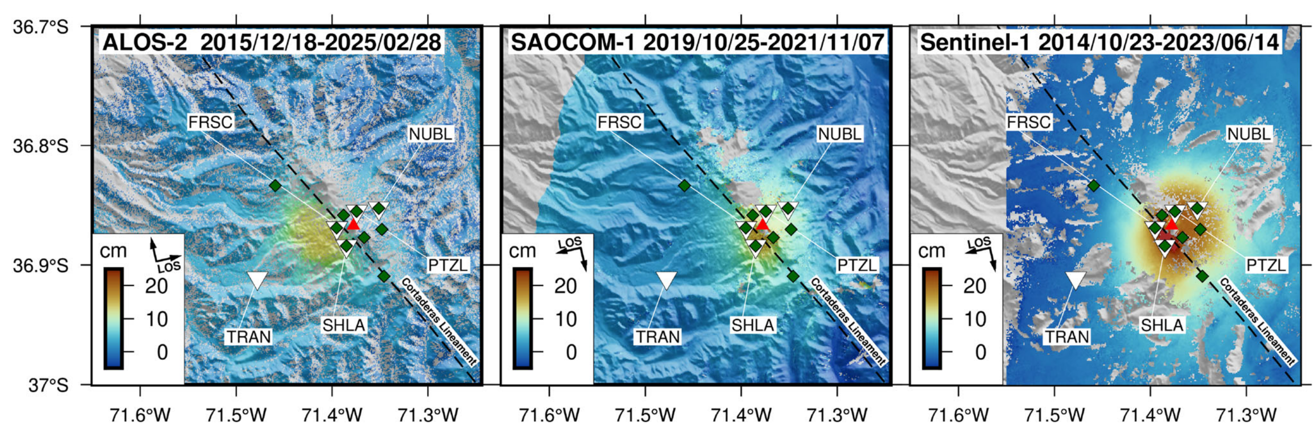

Fig. 5 Map of accumulated LOS displacement from ALOS-2 (ascending), SAOCOM-1, and Sentinel-1 (descending). Red colors indicate movement towards the satellite. The black dashed line marks the Cortaderas Lineament. Note the slightly different observation periods. Other features as in Fig. 1

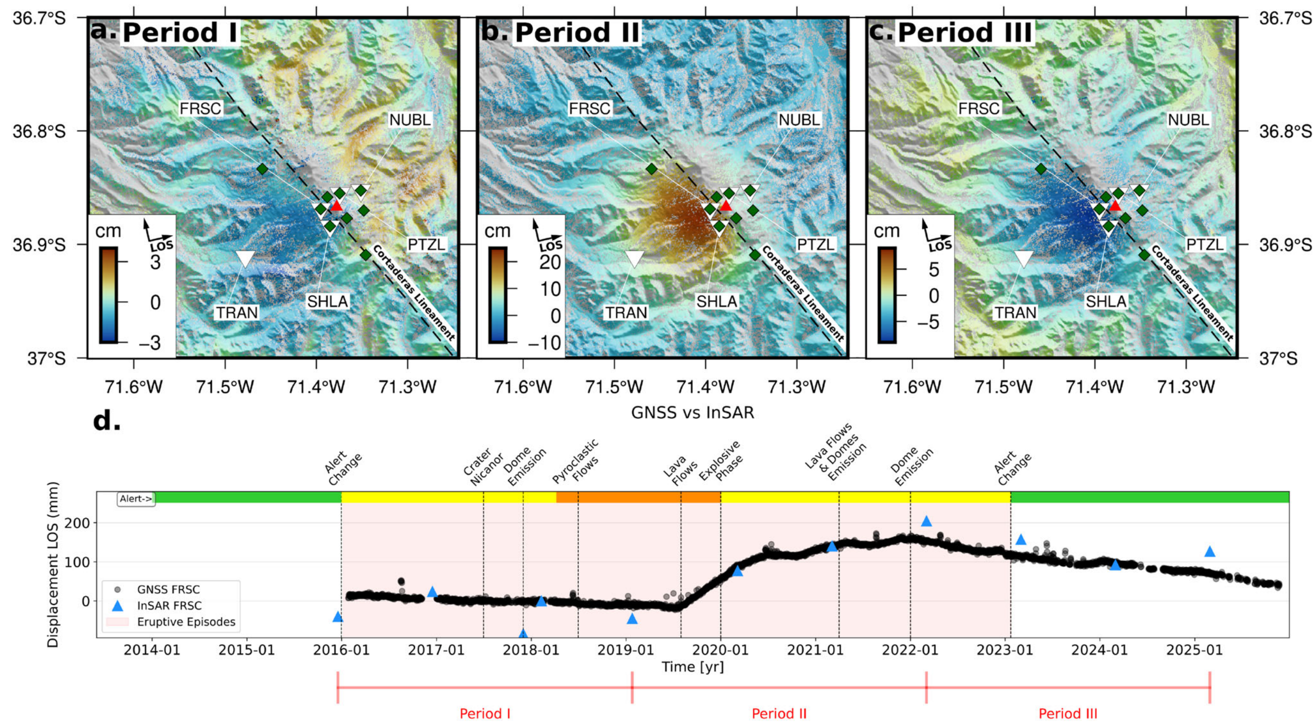

Fig. 6 Cumulative LOS displacement observed by ALOS-2 for three periods: **a** Period I: 2015/12/18–2019/01/25, **b** Period II: 2019/01/25–2022/03/04, and **c** Period III: 2022/03/04–2025/02/28. The black dashed line marks the Cortaderas Lineament. Other features as in Fig. 1. **d** Line-of-sight (LOS) displacement time series at station FRSC comparing GNSS (black dots) and ALOS-2 InSAR (light blue triangles), both referenced to CHTC, over the full observation period, with Sernageomin-OVDAS alert levels and eruptive episodes as in Fig. 2

SAOCOM-1, compared to the maximum displacement of ~25 cm. Residuals locally reach approximately ±2 cm on the SW flank. The comparison between predicted and observed GNSS horizontal velocities shows good first-order agreement, particularly at PTZL, TRAN, and NUBL (Fig. 7).

Forward model calculations using the same fixed geometry for Period I and Period III result in RMS residuals of 0.9 cm and 1.3 cm, respectively (Fig. 8). The forward-modeled horizontal GNSS velocities for Periods I and III are also compared with the observations in Fig. 8, and reproduce the first-order magnitude and orientation of the observations at most stations in both periods, with residuals of similar order to those obtained for Period II. Wrapped versions of the observed, modeled, and residual deformation are shown in Fig. S8.

Discussion

The geodetic and seismic observations at NChVC between 2015 and late 2025 define a three-period deformation cycle in which, despite sign changes in deformation between periods, the overall spatial pattern of deformation and seismicity remained broadly consistent through time. Forward calculations for Periods I and III using the preferred source geometry constrained during Period II reproduce the dominant spatial pattern of the observations, with RMS residuals of 0.9 and 1.3 cm, respectively (Fig. 8). This consistency indicates that deformation throughout the recent eruptive cycle was mainly associated with a shallow source region centered at approximately 5.4 km depth, though it does not rule out contributions from secondary or transiently active parts of the plumbing system. Differences in deformation amplitude and the localized residuals may reflect modest temporal variations in source dimensions, depth, or pressure conditions within this region. Nevertheless, the preferred Period II geometry reproduces most of the observed geodetic deformation and its first-order spatial pattern across the three periods.

The source depth of ~5.4 km (Fig. 9) is consistent with the thermobarometric constraints of Oyarzun et al. (2022), who estimated crystallization depths of dacitic and rhyodacitic magmas at NChVC between 2.2 and 9.7 km based on pre-eruptive Pleistocene–Holocene volcanic rocks. The inferred spheroid thus lies within this petrologically defined storage range, consistent with a shallow magma accumulation zone within a broader, vertically zoned plumbing system that need not have been entirely active during the observation period.

Previous studies inferred shallow deformation sources using different datasets, observation periods, and modeling approaches (Fig. 9). Despite these differences, most

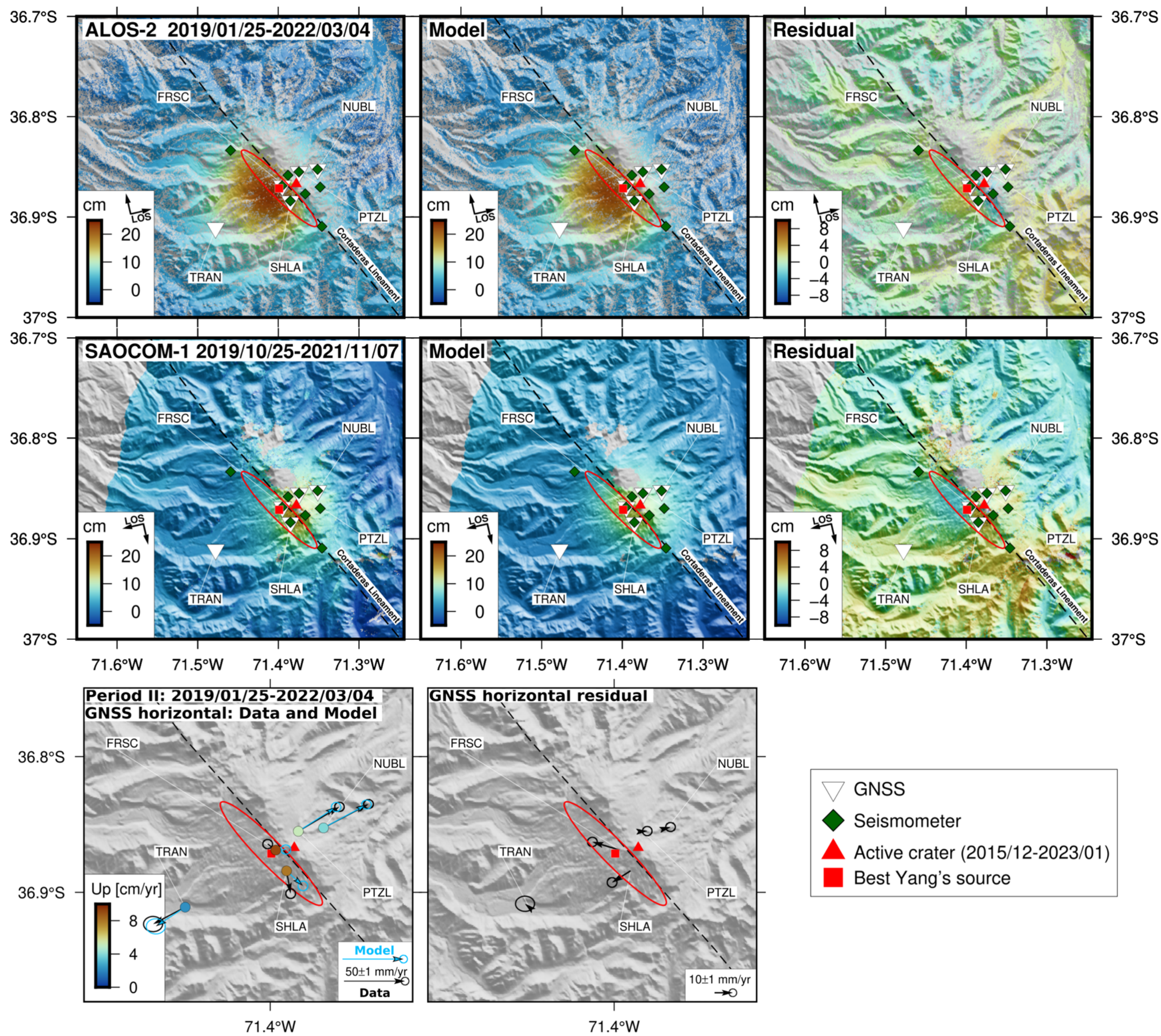

Fig. 7 Observed (left), predicted (center), and residual (right) deformation for the ALOS-2 (top) and SAOCOM-1 (middle) displacement maps during Period II. The prolate spheroid source is shown in all panels. The black dashed line marks the Cortaderas Lineament. Other features are as in Fig. 1. The lowest panels show the corresponding GNSS results for Period II (2019/01/25–2022/03/04). In the left GNSS panel, black and blue vectors represent the observed and predicted horizontal velocities, respectively, while the colored circles represent the observed vertical (Up) velocities in centimeters per year. The vertical-velocity color scale ranges from 0 to 10 cm/yr. The ellipses indicate the horizontal GNSS uncertainties. The right GNSS panel shows the horizontal residual velocities. Reference vector scales are indicated within each GNSS panel

estimates place the principal deformation source at approximately 4–6 km depth. Astort et al. (2022) inverted cumulative Sentinel-1 displacement maps from October 2019 to November 2020 and obtained a prolate spheroid at 5.5 ± 0.5 km depth, oriented along the NW–SE Cortaderas Lineament (Cardona et al. 2021; Mura et al. 2025). Lizama et al. (2025) combined ascending ALOS-2, descending Sentinel-1, and GNSS time series from January 2019 to May 2020, proposing a two-reservoir system composed of a shallow source at ∼5.8 km, accounting for ∼97% of the modeled uplift, and a deeper sill at ∼15 km contributing the remainder. Eiden et al. (2025) applied a Bayesian inversion framework using InSAR and GNSS for Uplift 1 and GNSS-only observations for subsequent periods, obtaining source depths of 4.3 ± 0.2 km, 4.8 ± 0.1 km, and 6.4 ± 0.5 km across the three deformation episodes.

Our results are spatially consistent with the principal shallow deformation sources identified in previous studies,

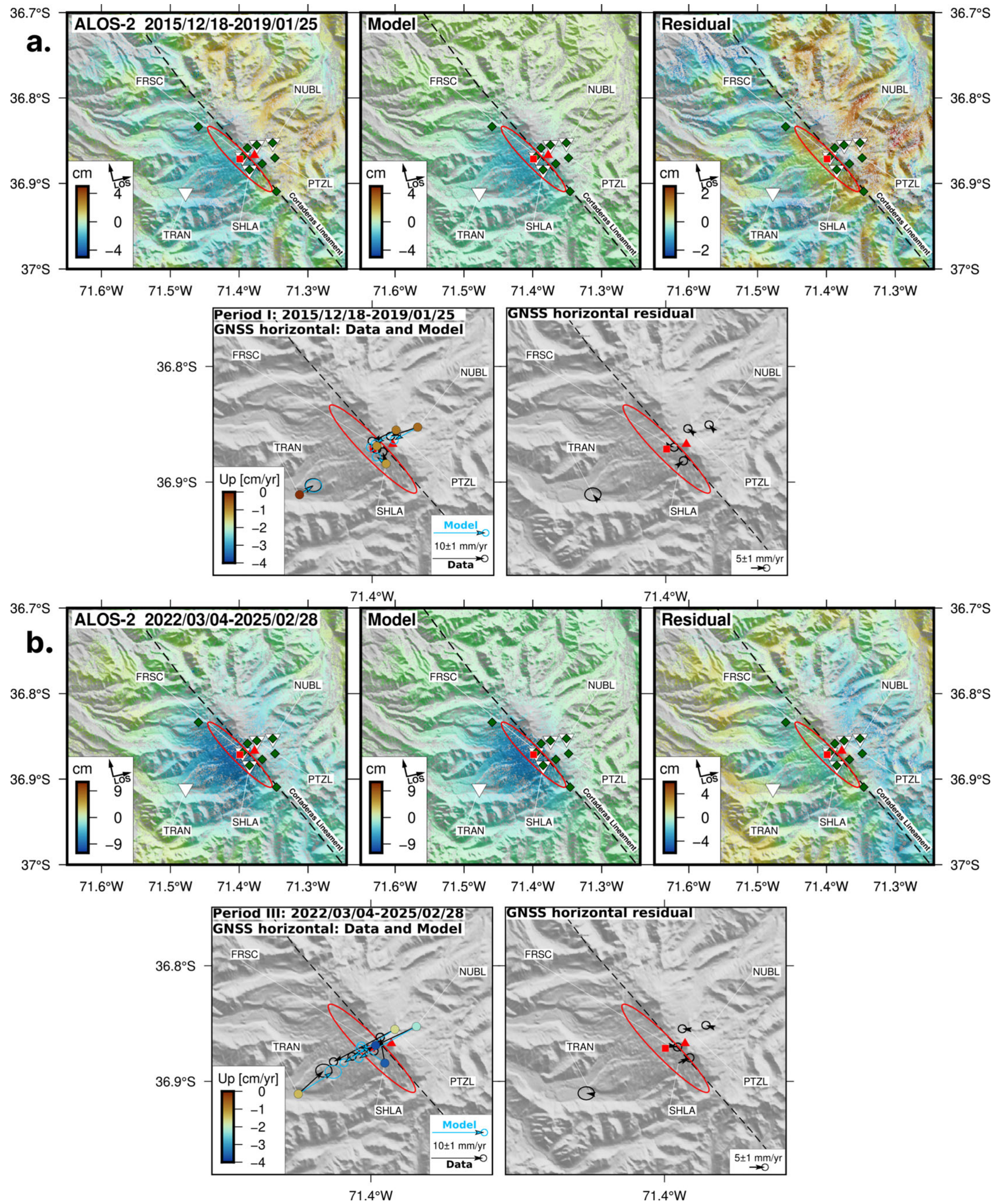

Fig. 8 Observed (left), predicted (center), and residual (right) ALOS-2 LOS displacements for **a**) Period I (2015/12/18–2019/01/25) and **b**) Period III (2022/03/04–2025/02/28), calculated using the preferred prolate spheroid geometry constrained during Period II. The corresponding GNSS results for each period are shown in the panels below the InSAR results. In the left GNSS panels, black and blue vectors represent the observed and predicted horizontal velocities, respectively, while the colored circles represent the observed vertical (Up) velocities in centimeters per year. Periods I and III use the same vertical-velocity color scale, ranging from −4 to 0 cm/yr. The ellipses indicate the horizontal GNSS uncertainties. The right GNSS panels show the horizontal residual velocities. Reference vector scales are indicated within each GNSS panel. Other features are as in Fig. 1

despite differences in datasets, source geometries, and modeling approaches. Our preferred spheroid overlaps the source inferred by Astort et al. (2022), the shallow source regions obtained by Eiden et al. (2025), and the shallow, dominant source proposed by Lizama et al. (2025) (Fig. 9). Only the deeper sill proposed by Lizama et al. (2025), at approximately 15 km depth, lies outside this shared shallow source region. However, this deeper source accounted for only

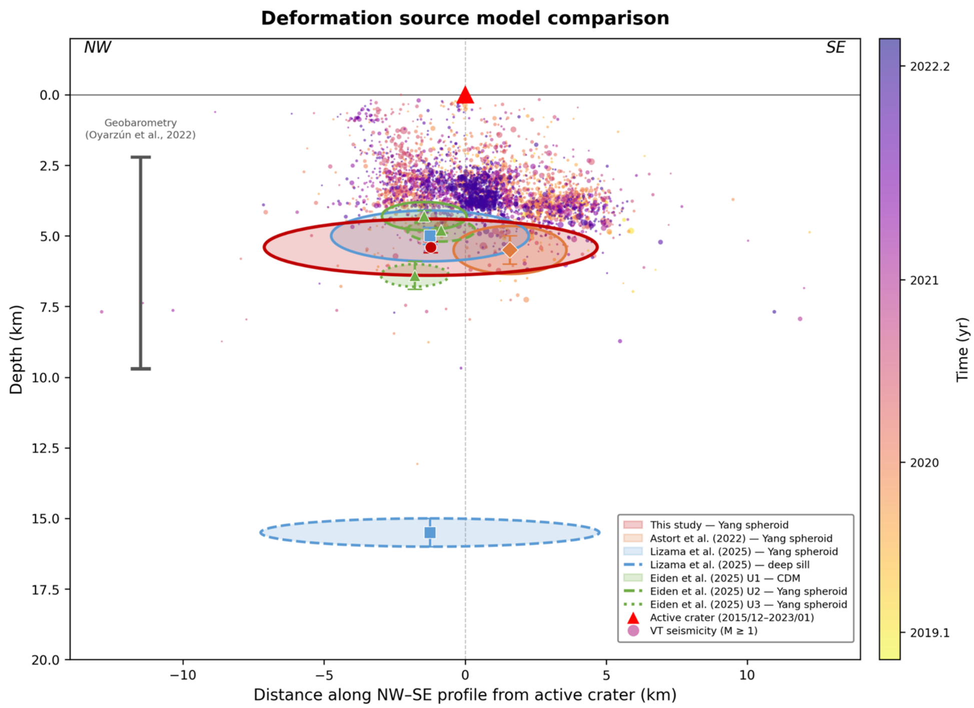

Fig. 9 Comparison of various volcanic source models (ellipses) along a NW–SE (N134°E) cross-section through the active Nicanor crater (red triangle). Vertical bars on each source indicate depth uncertainties (1σ). Small circles show volcano-tectonic (VT) seismicity from Period II (2019-01-25 to 2022-03-04) within 10 km of the profile ($\sim$99.5% of Period II events), colored by occurrence time and scaled by magnitude ($M \geq 1$). The gray bar on the left marks the depth range of magma storage inferred from geobarometry (Oyarzun et al. 2022). Note that some source geometries are shown schematically due to unreported parameters or limited observational constraints

approximately 3% of the modeled uplift, whereas the shallow source explained the remaining 97%. Although our observations cannot exclude deeper magma transfer or secondary components of the plumbing system, the shallow source reproduces most of the observed deformation and its first-order spatial pattern. Our source also shows a markedly larger lateral extent than those proposed in previous studies, with a major semi-axis of 5.9 ± 0.1 km (Fig. 9). This broader modeled footprint may partly reflect the wider coherent coverage provided by the L-band ALOS-2 observations. By preserving coherence across the vegetated flanks and farther from the active crater, the ALOS-2 interferograms sample a larger fraction of the deformation field and provide additional constraints on its long-wavelength component and lateral dimensions.

Taken together, these independent studies consistently place the principal deformation source at approximately 4–6 km depth. This agreement indicates that the shallow magmatic system played a central role in surface deformation during the recent eruptive cycle. The different source geometries shown in Fig. 9 may represent different parameterizations of a structurally and geometrically complex shallow storage system, rather than different volcanological interpretations. This interpretation is further supported by the concentration of Period II VT seismicity at approximately 3–6 km depth and by the independent magma-storage range inferred from geobarometry (Fig. 9). Together, the geodetic models, seismicity, and petrological constraints indicate that this shallow magmatic region was the main contributor to the observed deformation and eruptive activity.

The contrast between our predicted volume change of 0.048 km^3 and the relatively small erupted volumes of 0.01–0.02 km^3 (Servicio Nacional de Geología y Minería (SERNAGEOMIN) 2026) could suggest continued pressurization during eruption rather than simple depletion of a closed reservoir. This hypothesis is supported by the continuation of inflation throughout the main effusive phase. A pressurized shallow reservoir likely persisted during the main eruptive period. The vertical component at TRAN shows the same general inflationary trend during this interval (Figs. 4 and S3). Uplift at TRAN decays exponentially, a pattern known from magma injections modeled as a Newtonian fluid without crystals, in which the inflation rate decreases as the pressure difference between the source and the conduit equilibrates (Lengliné et al. 2008; Pinel et al. 2010). The relative contributions of magma supply, storage, compressibility, and eruptive output cannot be resolved in detail with the available observations, however.

During Period I, phreatic and phreatomagmatic explosions were followed by dome extrusion, repeated dome destruction, and pyroclastic flows, while the geodetic observations showed only subtle subsidence (Fig. 4). The contrast between the marked surface activity and the weak deformation suggests that this early stage may have been dominated by shallow hydrothermal and conduit processes, including degassing and the transfer of limited magma volumes toward the surface.

During Period II, the continuous GNSS data and the Sentinel-1 time series show that inflation was not uniform (Figs. 4 and S5). Following the subtle subsidence observed during Period I and the first months of 2019, uplift began in mid-2019 and increased rapidly through early 2020, coincident with a marked increase in seismicity and the emplacement of the first lava flows. This was followed by intervals of slower uplift and renewed increases through early 2022. The annual ALOS-2 observations at the near-source stations are consistent with this longer-term evolution, although their temporal sampling does not resolve the shorter-term variations visible in the GNSS and Sentinel-1 data.

A second prominent increase in LP and TR seismicity during 2021–2022 accompanied renewed dome growth, lava effusion, and the highest eruptive rates, broadly coinciding with the final stage of inflation. However, the timing and amplitude of the seismic, eruptive, and geodetic changes do not show a simple one-to-one correspondence. These differences suggest that the shorter-term fluctuations may reflect changes in magma and fluid transfer toward the surface and in eruptive discharge, superimposed on the longer-term pressurization of the dominant shallow source region identified by our model. The deformation subsequently reversed to deflation during Period III.

The VT seismicity supports a structural control on magma storage and migration. From 2018 onward, hypocenters aligned along a NW-SE trend consistent with the NW-SE lineament of NChVC (e.g., Cardona et al., 2021; Mura et al., 2025; Espinosa-Leal et al., 2025). During Period II they migrated ~3 km northeastward, culminating in the January 2022 cluster that coincided with increased LP activity (Figs. 2, 3, and S1). Most VT events occurred at 3–6 km depth and agree well with our predicted centroid source depth. Together with the alignment of eruptive centers, this spatial pattern points to a structural control on shallow magma storage and on the pathways of magma and fluids. The b-positive parameter showed no systematic variation correlated with surface deformation or seismic event rate throughout the cycle.

The horizontal displacement time series at station FRSC, located directly above the modeled source region, remained largely unaffected by the inflation. The slight decaying trajectory observed over the full observation period may include a far-field postseismic component associated with the 2010 Maule earthquake. We assessed this potential contribution using the regional interseismic deformation and viscoelastic relaxation predictions of Li et al. (2017, 2018). This assessment indicates that the predicted differential regional contribution between CHTC and the other GNSS stations is small, supporting the use of CHTC as a local reference and limiting the influence of Maule-related deformation on the relative GNSS time series. A rigorous separation of the regional and volcanic signals would require a dedicated analysis and is beyond the scope of the present study.

The coseismically induced subsidence at NChVC following the 2010 Maule earthquake was attributed to the release of hydrothermal fluids at 3–10 km depth (Pritchard et al. 2013). To evaluate whether this earthquake-related deformation could be reproduced by the same shallow source geometry inferred for the recent eruptive cycle, we applied the preferred Period II geometry to an ENVISAT interferogram spanning 2010/01/30–2010/04/10 (Pritchard et al. 2013). It should be noted that the ENVISAT interferogram may also include an early postseismic contribution, as the earthquake occurred on 27 February 2010 and the second acquisition was obtained on 10 April 2010. Figure S9 compares the observed LOS displacement, the forward-model prediction, and the corresponding residuals. The Period II geometry does not reproduce the observed spatial pattern of subsidence, indicating that the 2010 deformation cannot be explained by the same source geometry responsible for the deformation during Periods I–III. This result is consistent with the interpretation of Pritchard et al. (2013) that the 2010 subsidence reflected a hydrothermal rather than magmatic process. Similar non-eruptive subsidence unrelated to lava-flow dynamics has been documented at other volcanic systems, including Medicine Lake (Poland et al. 2006), Askja (De Zeeuw-van Dalfsen et al. 2012), Lassen Volcanic Center (Parker et al. 2016), and Cerro Blanco (Velez et al. 2021). Deflation and seismicity declined progressively through late 2025, extending the observations beyond previous studies at NChVC. Both deformation rate and seismicity decreased over time, pointing to gradual depressurization and a transition toward pre-eruptive background conditions. The continuation of slowly reducing deformation and seismicity through late 2025 demonstrates that system relaxation persisted well beyond the end of the eruptive cycle.

Conclusions

Ten years of seismo-geodetic time-series document one complete eruptive cycle (pre-, syn-, and post-eruptive Period I, II and III) of the Nevados de Chillán Volcanic Complex in Chile. This unique dataset combines a seismic catalog of long-period, tremor, and volcano-tectonic events and b-positive parameters with space- and in-situ-geodetic observations in three dimensions at millimeter sensitivity, and constitutes one of the most comprehensively documented eruptive sequences in the Southern Volcanic Zone.

During Period II (2019–2022), surface uplift peaked at ~25 cm along LOS. A shallow source at 5.4 ± 0.2 km depth reproduces the observed deformation with RMS residuals of 1.5 cm (ALOS-2) and 1.6 cm (SAOCOM-1). The modeled volume change of 0.048 km^3 exceeds the estimated eruptive lava volumes of 0.01–0.02 km^3 (Servicio Nacional de Geología y Minería (SERNAGEOMIN) 2026) by a factor of 2 to 4, suggesting that a pressurized shallow reservoir persisted throughout the eruptive period rather than progressively depleting. Volcano-tectonic seismicity migrated ~3 km northeastward during Period II and occurred predominantly at 3–6 km depth, consistent with the centroid depth of the modeled source. Together with the alignment of eruptive centers along the Cortaderas Lineament, this spatial pattern is suggestive of structural control on shallow magma storage and transport pathways.

The preferred Period II source geometry reproduces the deformation observed during Periods I and III through forward calculations, with RMS residuals of 0.9 cm (Period I) and 1.3 cm (Period III). Subsidence observed just after the 2010 Maule earthquake, however, is not reproduced by this geometry and is consistent with a distinct source of hydrothermal origin.

Deformation rates and seismicity declined gradually through late 2025, demonstrating that system relaxation persisted well beyond the end of the eruptive cycle. Our observations highlight the value of sustained multi-dataset monitoring over full eruptive cycles for constraining magmatic source evolution and informing volcanic hazard assessment.

Supplementary material

Supplementary File Supplementary.pdf is attached to this submission.

Supplementary Information The online version contains supplementary material available at https://doi.org/10.1007/s00445-026-02032-1.

Acknowledgements We thank CSN, Sernageomin and the OVDAS team for providing seismic and GNSS data.

Author contributions Conceptualization: B.S.L., F.D., S.M., and S.R.
Methodology: B.S.L., F.D., and S.R.
Data curation: B.S.L., F.D., L.C., J.C.B, and A.A.
Visualization: B.S.L.
Writing—original draft: B.S.L.
Writing—review and editing: all authors
Funding acquisition: B.S.L., S.R., and J.C.B.
Resources: S.R., J.C.B., F.D., L.C., S.L., and A.A.
Supervision: F.D., S.M., and S.R.

Funding Open Access funding enabled and organized by Projekt DEAL. B.S.L. acknowledges the support of the National Research and Development Agency (ANID)/Scholarship Program/DOCTORADO BECAS CHILE/2023-72230401.
S.R. and J.C.B. acknowledge the support of ANID-FONDECYT Projects 1240501 and 1262157.
L.C. acknowledges the support of the Center for Interdisciplinary Research on Disaster Risk, Resilience and Recovery (CIGIDEN R+), ANID/CIN250023.
F.D. thanks JAXA (Japan Aerospace Exploration Agency) for providing ALOS-2 data through the EO-RA4 ER4A2N060 project. This study was funded by ANID-FONDECYT Regular Grant 1251171.

Data availability Global Navigation Satellite System (GNSS) and seismic data were obtained through the Southern Andes Volcano Observatory (Observatorio Volcanológico de los Andes del Sur, OVDAS), in collaboration with the National Seismological Center (Centro Sismológico Nacional, CSN) of the Universidad de Chile (see http://gnss.csn.uchile.cl). Access to the original OVDAS data must be requested from this institution. Interferometric Synthetic Aperture Radar (InSAR) data from the Sentinel-1 mission are available via the COMET-LiCS Sentinel-1 InSAR portal (https://comet.nerc.ac.uk/comet-lics-portal/). ALOS-2 satellite data were provided by the Japan Aerospace Exploration Agency (JAXA) through the G-Portal data service, SAOCOM-1 data were provided by the Comisión Nacional de Actividades Espaciales (CONAE), and the Copernicus Digital Elevation Model (DEM) was provided by the European Space Agency (ESA). The Generic Mapping Tools (GMT) were used for data visualization.

Materials availability Not applicable.

Code availability Not applicable.

Declarations

Ethical approval and consent to participate Not applicable.

Consent for publication Not applicable.

Competing interests The authors declare no competing interests.

Open Access This article is licensed under a Creative Commons Attribution 4.0 International License, which permits use, sharing, adaptation, distribution and reproduction in any medium or format, as long as you give appropriate credit to the original author(s) and the source, provide a link to the Creative Commons licence, and indicate if changes were made. The images or other third party material in this article are included in the article's Creative Commons licence, unless indicated otherwise in a credit line to the material. If material is not included in the article's Creative Commons licence and your intended use is not permitted by statutory regulation or exceeds the permitted use, you will need to obtain permission directly from the copyright holder. To view a copy of this licence, visit http://creativecommons.org/licenses/by/4.0/.

References

Astort A, Boixart G, Folguera A, Battaglia M (2022) Volcanic unrest at Nevados de Chillán (southern Andean volcanic zone) from January 2019 to November 2020, imaged by DInSAR. J Volcanol Geoth Res 427. https://doi.org/10.1016/j.jvolgeores.2022.107568

Báez JC, Leyton F, Troncoso C, Del Campo F, Bevis M, Vigny C, Moreno M, Simons M, Kendrick E, Parra H et al (2018) The Chilean GNSS network: current status and progress toward early warning applications. Seismol Res Lett 89(4):1546–1554. https://doi.org/10.1785/0220180011

Brüggen J (1948) Contribución a la geología de los volcanes y termas de chillán

Cabrera L, Ardid A, Melchor I, Ruiz S, Symmes-Lopetegui B, Carlos Báez J, Delgado F, Martinez-Yáñez P, Dempsey D, Cronin S (2024) Eruption forecasting model for Copahue volcano (southern Andes) using seismic data and machine learning: a joint interpretation with geodetic data (GNSS and InSAR). Seismol Res Lett 95(5):2595–2610. https://doi.org/10.1785/0220240022

Cardona C, Gil-Cruz F, Franco-Marín L, San Martín J, Valderrama O, Lazo J, Cartes C, Morales S, Hernández E, Quijada J et al (2021) Volcanic activity accompanying the emplacement of dacitic lava domes and effusion of lava flows at Nevados de Chillán volcanic complex-Chilean Andes (2012 to 2020). J Volcanol Geoth Res 420. https://doi.org/10.1016/j.jvolgeores.2021.107409

Chen CW, Zebker HA (2002) Phase unwrapping for large SAR interferograms: statistical segmentation and generalized network models. IEEE Trans Geosci Remote Sens 40(8):1709–1719. https://doi.org/10.1109/TGRS.2002.802453

Cortés J, Gertisser R, Calder E (2024) Magma recharge in persistently active basaltic-andesite systems and its geohazards implications: the case of Villarrica volcano, Chile. Int J Earth Sci 113(5):1145–1163. https://doi.org/10.1007/s00531-024-02414-w

Dach R, Bock H, Fridez P, Gäde A, Hugentobler UP, Jäggi A, Mervart L, Meindl M, Schaer S, Urschl C (2007) Bernese GPS software

De Zeeuw-van Dalfsen E, Pedersen R, Hooper A, Sigmundsson F (2012) Subsidence of Askja caldera 2000–2009: modelling of deformation processes at an extensional plate boundary, constrained by time series InSAR analysis. J Volcanol Geoth Res 213:72–82. https://doi.org/10.1016/j.jvolgeores.2011.11.004

Delgado F, Pritchard ME, Ebmeier S, González P, Lara L (2017) Recent unrest (2002–2015) imaged by space geodesy at the highest risk Chilean volcanoes: Villarrica, Llaima, and Calbuco (southern Andes). J Volcanol Geoth Res 344:270–288. https://doi.org/10.1016/j.jvolgeores.2017.05.020

Delgado F, Shreve T, Borgstrom S, León-Ibanez P, Poland M et al (2024) A global assessment of SAOCOM-1 L-band stripmap data for InSAR characterization of volcanic, tectonic, cryospheric, and anthropogenic deformation. IEEE Trans Geosci Remote Sens. https://doi.org/10.1109/TGRS.2024.3423792

Delgado F, León-Ibáñez P, Báez JC, Parra S (2025) The triggering of sub-Plinian and Plinian eruptions: insights from three decades of InSAR observations in the Andean Southern Volcanic Zone (1991–2025) and a global compilation. J Geophys Res Solid Earth 130(12):2025–032010. https://doi.org/10.1029/2025JB032010

Dixon HJ, Murphy MD, Sparks SJ, Chavez R, Naranjo JA, Dunkley PN, Young SR, Gilbert JS, Pringle MR (1999) The geology of Nevados de Chillán volcano, Chile. Revista geológica de Chile 26(2):227–253. https://doi.org/10.4067/S0716-02081999000200006

Eiden E, Pritchard ME, Lundgren P, Córdova L, Cardona C, Bato MG, Moussallam Y, Gomez-Patron A, Barnie T, Amigo A (2025) Understanding the changing dynamics of the 2016–2022 Nevados de Chillán, Chile eruption through erupted volume and surface deformation. Bull Volcanol 87(9):71. https://doi.org/10.1007/s00445-025-01861-w

Espinosa-Leal J, Browning J, Cembrano J, Mitchell T, Rojas F, Moorkamp M, Griffith WA, Meredith P (2025) Fault intersection-related stress rotation controls magma emplacement at the Nevados de Chillán volcanic complex. J Volcanol Geoth Res 458:108255. https://doi.org/10.1016/j.jvolgeores.2024.108255

Farr TG, Rosen PA, Caro E, Crippen R, Duren R, Hensley S, Kobrick M, Paller M, Rodriguez E, Roth L et al (2007) The shuttle radar topography mission. Reviews of Geophysics 45(2). https://doi.org/10.1029/2005RG000183

Galetto F, Pritchard ME, Hornby AJ, Gazel E, Mahowald NM (2023) Spatial and temporal quantification of subaerial volcanism from 1980 to 2019: solid products, masses, and average eruptive rates. Rev Geophys 61(1):2022–000783. https://doi.org/10.1029/2022RG000783

Goldstein RM, Werner CL (1998) Radar interferogram filtering for geophysical applications. Geophys Res Lett 25(21):4035–4038. https://doi.org/10.1029/1998GL900033

Gomba G, Parizzi A, De Zan F, Eineder M, Bamler R (2015) Toward operational compensation of ionospheric effects in SAR interferograms: the split-spectrum method. IEEE Trans Geosci Remote Sens 54(3):1446–1461. https://doi.org/10.1109/TGRS.2015.2481079

Heap MJ, Villeneuve M, Albino F, Farquharson JI, Brothelande E, Amelung F, Got J-L, Baud P (2020) Towards more realistic values of elastic moduli for volcano modelling. J Volcanol Geoth Res 390:106684. https://doi.org/10.1016/j.jvolgeores.2019.106684

Lara L, Orozco G, Amigo A, Silva C (2011) Peligros volcánicos de chile, servicio nacional de geología y minería, carta geológica de chile. Santiago,(no. 13: 34 p., 1 mapa escala 1: 2.000. 000 serie geología ambiental)

Lazeckỳ M, Spaans K, González PJ, Maghsoudi Y, Morishita Y, Albino F, Elliott J, Greenall N, Hatton E, Hooper A et al (2020) LiCSAR: an automatic InSAR tool for measuring and monitoring tectonic and volcanic activity. Remote Sens 12(15):2430. https://doi.org/10.3390/rs12152430

Le Mével H, Córdova L, Cardona C, Feigl K (2021) Unrest at the Laguna del Maule volcanic field 2005–2020: renewed acceleration of deformation. Bull Volcanol 83(6):39. https://doi.org/10.1007/s00445-021-01457-0

Lengliné O, Marsan D, Got J-L, Pinel V, Ferrazzini V, Okubo PG (2008) Seismicity and deformation induced by magma accumulation at three basaltic volcanoes. J Geophys Res 113:12305. https://doi.org/10.1029/2008JB005937

Li S, Moreno M, Bedford J, Rosenau M, Heidbach O, Melnick D, Oncken O (2017) Postseismic uplift of the Andes following the 2010 Maule earthquake: Implications for mantle rheology. Geophys Res Lett 44(4):1768–1776. https://doi.org/10.1002/2016GL071995

Li S, Bedford J, Moreno M, Barnhart WD, Rosenau M, Oncken O (2018) Spatiotemporal variation of mantle viscosity and the presence of cratonic mantle inferred from 8 years of postseismic deformation following the 2010 Maule, Chile, earthquake. Geochem Geophys Geosyst 19(9):3272–3285. https://doi.org/10.1029/2018GC007645

Liang C, Fielding EJ (2017a) Interferometry with ALOS-2 full-aperture ScanSAR data. IEEE Trans Geosci Remote Sens 55(5):2739–2750. https://doi.org/10.1109/TGRS.2017.2653190

Liang C, Fielding EJ (2017b) Measuring azimuth deformation with L-band ALOS-2 ScanSAR interferometry. IEEE Trans Geosci Remote Sens 55(5):2725–2738. https://doi.org/10.1109/TGRS.2017.2653186

Liang C, Liu Z, Fielding EJ, Bürgmann R (2018) InSAR time series analysis of L-band wide-swath SAR data acquired by ALOS-2. IEEE Trans Geosci Remote Sens 56(8):4492–4506. https://doi.org/10.1109/TGRS.2018.2821150

Lizama CN, Remy D, Baez J, Oyarzun A, Bonvalot S, Hooper A (2025) Modeling magma recharge dynamics during the 2016 Nevados de Chillan eruption: an interacting two-chamber system evidenced by petrology and geodesy. J Volcanol Geoth Res 458:108253. https://doi.org/10.1016/j.jvolgeores.2024.108253

Lohman RB, Simons M (2005) Some thoughts on the use of InSAR data to constrain models of surface deformation: noise structure and data downsampling. Geochemistry, Geophysics, Geosystems 6(1). https://doi.org/10.1029/2004GC000841

Maldonado V, Contreras M, Melnick D (2021) A comprehensive database of active and potentially-active continental faults in Chile at 1:25,000 scale. Scientific Data 8:20

Moreno M, Melnick D, Rosenau M, Baez J, Klotz J, Oncken O, Tassara A, Chen J, Bataille K, Bevis M, Socquet A, Bolte J, Vigny C, Brooks B, Ryder I, Grund V, Smalley B, Carrizo D, Bartsch M, Hase H (2012) Toward understanding tectonic control on the mw 8.8 2010 Maule Chile earthquake. Earth Planet Sci Lett 321–322:152–165. https://doi.org/10.1016/j.epsl.2012.01.006

Morishita Y, Lazecky M, Wright TJ, Weiss JR, Elliott JR, Hooper A (2020) LiCSBAS: an open-source InSAR time series analysis package integrated with the LiCSAR automated Sentinel-1 InSAR processor. Remote Sens 12(3):424. https://doi.org/10.3390/rs12030424

Moussallam Y, Bani P, Schipper CI, Cardona C, Franco L, Barnie T, Amigo Á, Curtis A, Peters N, Aiuppa A et al (2018) Unrest at the Nevados de Chillán volcanic complex: a failed or yet to unfold magmatic eruption? Volcanica 1(1):19–32. https://doi.org/10.30909/vol.01.01.1932

Mura V, Arancibia G, Browning J, Healy D, López-Contreras C, Morata D, Maza S, Cardona C (2025) Structural control on the southern Andean Nevados de Chillán geothermal system. Journal of Structural Geology 105380. https://doi.org/10.1016/j.jsg.2025.105380

Naranjo JA, Gilbert J, Sparks SJ (2008) Geología del complejo volcánico Nevados de Chillán, región del bío bío

Naranjo J, Moreno H (2009) Reciente erupción en el complejo volcánico Nevados de Chillán, región del biobío. In: XII Congreso Geológico Chileno, Santiago, Actas, vol 3, p 016

Naranjo J, Chávez R, Sparks R, Gilbert J, Dunkley P (1994) Nuevos antecedentes sobre la evolución cuaternaria del complejo volcánico nevados de chillán. Congreso Geológico Chileno 7:342–345

Navarrete-Reyes M, Delgado F, Ruiz S, Báez J, Potin B, Cabrera L, Alarcón A (2026) Long unrest (2007–2025) at Laguna del Maule: linking strain field and seismicity from GNSS and seismic data. Geophys Res Lett 53(4):2025–120184. https://doi.org/10.1029/2025GL120184

Orozco G, Jara G, Bertin D (2016) Peligros del complejo volcánico Nevados de Chillán.(región del biobío)

Oyarzun A, Lara LE, Tassara A (2022) Decoding the plumbing system of Nevados de Chillán volcanic complex, southern Andes. J Volcanol Geoth Res 422:107455. https://doi.org/10.1016/j.jvolgeores.2021.107455

Parker AL, Biggs J, Lu Z (2016) Time-scale and mechanism of subsidence at Lassen Volcanic Center, CA, from InSAR. J Volcanol Geoth Res 320:117–127. https://doi.org/10.1016/j.jvolgeores.2016.04.013

Pineda C, Arancibia G, Mura V, Morata D, Maza S, Browning J (2025) Mafic enclaves reveal multi-magma storage and feeding of Shangri-la Lavas at the Nevados de Chillán volcanic complex. Minerals 15(4):418. https://doi.org/10.3390/min15040418

Pinel V, Jaupart C, Albino F (2010) On the relationship between cycles of eruptive activity and growth of a volcanic edifice. J Volcanol Geoth Res 194:150–164. https://doi.org/10.1016/j.jvolgeores.2010.05.006

Poland M, Bürgmann R, Dzurisin D, Lisowski M, Masterlark T, Owen S, Fink J (2006) Constraints on the mechanism of long-term, steady subsidence at medicine lake volcano, Northern California, from GPS, leveling, and InSAR. J Volcanol Geoth Res 150(1–3):55–78. https://doi.org/10.1016/j.jvolgeores.2005.07.007

Pritchard M, Jay J, Aron F, Henderson S, Lara L (2013) Subsidence at southern Andes volcanoes induced by the 2010 Maule, Chile earthquake. Nat Geosci 6(8):632–636. https://doi.org/10.1038/ngeo1855

Radic JP (2010) Las cuencas cenozoicas y su control en el volcanismo de los complejos nevados de chillán y copahue-callaqui (Andes del sur, 36–39 s). Andean Geology 37(1):220–246. https://doi.org/10.4067/S0718-71062010000100009

Ramos VA, Folguera A (2005) Tectonic evolution of the Andes of Neuquén: constraints derived from the magmatic arc and foreland deformation. https://doi.org/10.1144/gsl.sp.2005.252.01.02

Ramos V, Barbieri M (1989) El volcanismo cenozoico de huantraico: edad y relaciones isotópicas iniciales, provincia del neuquén. Revista de la Asociación Geológica Argentina 43(2):210–223

Rosen PA, Gurrola E, Sacco GF, Zebker H (2012) The InSAR scientific computing environment. In: EUSAR 2012; 9th European Conference on Synthetic Aperture Radar, pp 730–733

Rosen PA, Hensley S, Chen C (2010) Measurement and mitigation of the ionosphere in l-band interferometric SAR data. 2010 IEEE Radar Conference. IEEE, pp 1459–1463. https://doi.org/10.1109/RADAR.2010.5494385

Servicio Nacional de Geología y Minería (SERNAGEOMIN) (2026) Red Nacional de Vigilancia Volcánica. Accessed 13 April 2026. https://www.sernageomin.cl/rnvv/

Simkin T (1994) Volcanoes of the world. Smithsonian Institution 349

Stanton-Yonge A, Griffith W, Cembrano J, St. Julien R, Iturrieta P (2016) Tectonic role of margin-parallel and margin-transverse faults during oblique subduction in the southern volcanic zone of the Andes: insights from boundary element modeling. Tectonics 35(9):1990–2013. https://doi.org/10.1002/2016TC004226

Stern CR (2004) Active Andean volcanism: its geologic and tectonic setting. Revista Geológica De Chile 31(2):161–206. https://doi.org/10.4067/S0716-02082004000200001

Van Der Elst NJ (2021) B-positive: a robust estimator of aftershock magnitude distribution in transiently incomplete catalogs. J Geophys Res Solid Earth 126(2):2020–021027. https://doi.org/10.1029/2020JB021027

Velez ML, Bustos E, Euillades L, Blanco M, López J, Barbero I, Berrocoso M, Martinez AG, Viramonte JG (2021) Ground deformation at the Cerro Blanco caldera: a case of subsidence at the Central Andes BackArc. J S Am Earth Sci 106:102941. https://doi.org/10.1016/j.jsames.2020.102941

Yang X-M, Davis PM, Dieterich JH (1988) Deformation from inflation of a dipping finite prolate spheroid in an elastic half-space as a model for volcanic stressing. J Geophys Res Solid Earth 93(B5):4249–4257. https://doi.org/10.1029/JB093iB05p04249

Yu C, Penna NT, Li Z (2017) Generation of real-time mode high-resolution water vapor fields from GPS observations. J Geophys Res Atmosph 122(3):2008–2025. https://doi.org/10.1002/2016JD025753

Yu C, Li Z, Penna NT, Crippa P (2018) Generic atmospheric correction model for interferometric synthetic aperture radar observations. J Geophys Res Solid Earth 123(10):9202–9222. https://doi.org/10.1029/2017JB015305

Yunjun Z, Fattahi H, Amelung F (2019) Small baseline InSAR time series analysis: unwrapping error correction and noise reduction. Comput Geosci 133:104331. https://doi.org/10.1016/j.cageo.2019.104331